Research Square

Preprints are preliminary reports that have not undergone peer review.
They should not be considered conclusive, used to inform clinical practice,
or referenced by the media as validated information.

Single-Projection Three-Dimensional X-ray Imaging through Time- and Energy-Resolved Photon Scattering

Shusen Jing
University of California-San Francisco
Qihui Lyu
University of California-San Francisco
Qifan Xu
University of California-San Francisco
Seungeun Lee
Lawrence Berkeley National Laboratory
Woon-Seng Choong
Lawrence Berkeley National Laboratory
Joshua Cates
Lawrence Berkeley National Laboratory
Ke Sheng
ke.sheng@ucsf.edu
University of California-San Francisco

Article

Keywords:

Posted Date: November 12th, 2026

DOI: https://doi.org/10.21203/rs.3.rs-11447801/v1

License: This work is licensed under a Creative Commons Attribution 4.0 International License.
Read Full License

Additional Declarations: No competing interests reported.

Single-Projection Three-Dimensional X-ray Imaging through Time- and Energy-Resolved Photon Scattering

Shusen Jing[1], Qihui Lyu[1], Qifan Xu[1], Seungeun Lee[2], Woon-Seng Choong[2], Joshua Cates[2], Ke Sheng[1]

1. Department of Radiation Oncology, University of California-San Francisco, San Francisco, CA 94115
2. Lawrence Berkeley National Laboratory, Berkeley, CA 94720

Corresponding author: Ke Sheng, Ph.D.

Professor and Vice Chair

Department of Radiation Oncology

University of California, San Francisco

Email: ke.sheng@ucsf.edu

Abstract

Scattered X-ray photons contain information about material composition but are generally treated as contamination in conventional computed tomography (CT). We investigate a theoretical time- and energy-encoded CT framework that uses photon arrival time, position, and energy to localize scattering events and reconstruct three-dimensional Rayleigh and Compton scattering distributions from a single projection without mechanical rotation. The framework was evaluated using Geant4 Monte Carlo simulations of heterogeneous tissue, head-and-neck, and high-resolution pattern phantoms. Under idealized source and detector conditions, the reconstructed scattering distributions differentiated soft tissues and reproduced simulated structures, including features as small as 0.1 mm. Quantitative errors of approximately 1–7% and a simulated dose of 50 μGy were reported for the investigated configurations. These results establish the information-reconstruction potential of time- and energy-resolved scatter measurements, rather than the performance of a realizable clinical scanner. Implementation will require ultrashort X-ray pulses, precise photon timing and energy measurements, and adequate detector coverage. The approach provides a theoretical basis for investigating single-projection volumetric X-ray scatter imaging and material characterization.

Introduction

Computed Tomography (CT) is an X-ray imaging modality that estimates the linear attenuation coefficient (LAC) of objects along their cross-sections. In the most widely used energy-integration mode, the attenuation of the X-ray beam intensity after passing through the object is measured along multiple paths. These measurements are then formulated into a system of linear equations based on the Beer–Lambert law [1], from which the cross-sectional LACs can be estimated. Computationally efficient methods, including filtered back projection, iterative reconstruction, and deep learning, have been developed for high-resolution and large field-of-view applications [2]. CT has become a cornerstone of modern imaging science and practice with wide applications in medicine, basic science, and industrial material inspection. Conventional CT image formation relies on the collection of primary photon signals that penetrate the scanning object without interacting with it. The unavoidable scattered photons from Compton and Rayleigh interactions are deemed contamination to the primary photon signals and a cause of image quality degradation.

The severity of scatter artifacts is strongly influenced by scanning geometry. In fan-beam CT, scatter is minimal because most scattered photons deviate away from the detector and are naturally rejected. As the beam geometry broadens, scatter artifacts increase and become most pronounced in cone-beam CT, which acquires volumetric images in a single source–detector rotation. Scattered photons lead to an overestimation of the exit signal intensity, resulting in characteristic distortions, such as cupping artifacts, and degraded contrast and resolution. These artifacts are further amplified in regions with high-density materials, where scattering increases with material density [3]. Over the past decades, considerable effort has been devoted to mitigating scatter contamination. Common approaches include anti-scatter grids [4,5], beam-pass or beam-stop filters [6–8] and iterative estimation of linear attenuation coefficients (LAC) and scatter using approximate scatter models[9 10]. In a recent theoretical paper, Time-of-Flight (TOF) detectors were modeled to filter out scattered photons, which travel longer paths to the detector [11].

Despite practical approaches to minimize scatter photon contributions in CT reconstruction, in theory, scatter photons interact with the object and carry unique information about the scanned object. A similar concept was exploited in the Compton camera, where Compton-scattered photons were used to estimate the location of the gamma-ray source [12,13]. This technique employs two detectors: one to induce Compton scattering and the other to record the energy of the scattered photons. For each Compton scattering event, it is possible to determine that the source lies on the surface of a cone, with the cone angle derived from the Klein–Nishina formula. Finally, the radioactive source distribution is derived based on the cone intersections. The concept of Compton Scatter Imaging (CSI) for constrained imaging geometry, where the X-ray source and detectors are on the same side of the object, was investigated[14,15]. The scatter photon energy was used to determine the scatter angle for image reconstruction. A related application of scatter photon imaging is real-time anatomical monitoring

during radiation therapy. For example, researchers [16] collect scattered photons produced by MV therapeutic beams interacting with tissue to image the lung tumor during stereotactic body radiation therapy (SBRT). CSI potentially provides major internal contours of the subjects, while higher-quality kV X-ray imaging is unattainable.

Other than these limited applications, the full information carried by scatter photons in kV X-ray imaging has not been thoroughly interrogated due to several technical challenges. Unlike the primary photons in energy-integration CT, the rich information carried by scatter photons can only be resolved by a high-temporal-resolution system, including an X-ray source with extremely short pulse widths and an ultrafast detector. More specific scatter photon detection requires a monochromatic X-ray source and a detector capable of quantifying incident photon energies. Some of the individual components for such a system have been developed for different purposes, e.g., time-of-flight (TOF) detectors for reconstruction-free PET[17], photon-counting CT with energy resolution[18], and photo-cathode X-ray sources with ps pulse widths [19]. However, alongside the significant efforts required to build a dedicated imaging system, the theoretical potential to fully exploit the rich spatiotemporal and spectral data from both primary and scattered photons must be understood. In this work, we present the theoretical framework for a novel time-energy-encoded (TEE) CT system designed to harness the full information content of both primary and scatter photons.

Results

Slab phantom

The slab phantom consists of five materials: water, muscle, adipose tissue, breast, and liver is placed at (0, 0, 310 mm)**.** The material properties are summarized in Table 1. Each material is represented by a slab of size 20 mm × 100 mm × 100 mm**.** They are stacked along the z-axis, making a 100 mm × 100 mm × 100 mm cube. A mono-energetic source at energies 100 keV is simulated, emitting cone-beams with a half-cone-angle of 12 degrees. The image voxel is of size 1 mm × 1 mm × 1 mm.

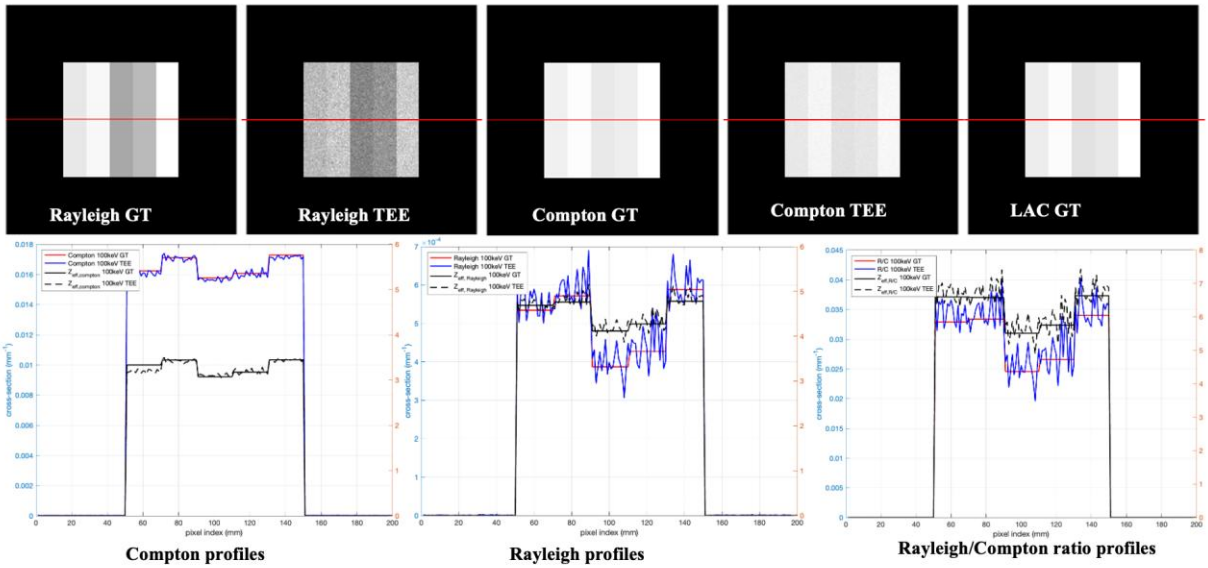


Figure 1. TEE reconstructed Rayleigh and Compton images of the slab phantom. The top and bottom rows show the images and profiles, respectively.

Figure 1 shows the TEE reconstruction results of the phantom. From this figure, we make the following observations: (1) The Rayleigh images exhibit higher contrast compared to the Compton images, as Compton scattering is approximately proportional to the material density, whereas Rayleigh scattering scales roughly with the square of the atomic number (Z_{eff}). (2) The LAC image closely resembles the Compton image, since Compton scattering dominates the linear attenuation coefficient (LAC) at this energy level. (3) The reconstructed Rayleigh image appears noisier than the Compton image, due to the significantly smaller Rayleigh scattering cross-section at this energy, which leads to a lower number of detected events. It is worth noting that the total dose delivered to the object is only 50 μGy due to the efficient use of photons for reconstruction.

MATERIALS	WATER	MUSCLE	ADIPOSE	BREAST	LIVER
RAYLEIGH GT (10^{-4} MM)	5.34	5.71	3.87	4.27	5.88
RAYLEIGH TEE (10^{-4} MM)	5.46 ± 0.3	5.83 ± 0.4	3.96 ± 0.3	4.38 ± 0.3	6.00 ± 0.4
RAYLEIGH TEE ERROR	5.60%	6.05%	6.89%	6.87%	5.22%
COMPTON GT (10^{-2} MM)	1.62	1.71	1.58	1.61	1.73
COMPTON TEE (10^{-2} MM)	1.61 ± 0.02	1.70 ± 0.02	1.56 ± 0.02	1.60 ± 0.02	1.71 ± 0.02
COMPTON TEE ERROR	1.09%	0.97%	1.00%	0.99%	1.10%
Σ_r / Σ_C GT (10^{-2})	3.29	3.34	2.46	2.66	3.40
Σ_r/Σ_C TEE (10^{-2})	3.39 ± 0.23	3.43 ± 0.25	2.53 ± 0.21	2.75 ± 0.22	3.51 ± 0.22
Σ_r / Σ_C ERROR	5.96%	6.34%	7.19%	7.18%	5.60%
$Z_{EFF,COMPTON}$	3.33	3.44	3.07	3.18	3.44
$Z_{EFF,COMPTON}$ TEE	3.20	3.40	3.08	3.18	3.43
$Z_{EFF,\ RAYLEIGH}$	4.69	4.76	4.12	4.28	4.78
$Z_{EFF,\ RAYLEIGH}$ TEE	4.67	4.80	4.17	4.31	4.85
$Z_{EFF,\ R/C}$	6.60	6.59	5.51	5.76	6.63
$Z_{EFF,\ R/C}$ TEE	6.66	6.71	5.60	5.87	6.81

Table 1 presents the reconstructed Rayleigh and Compton scattering cross-sections.

Table 1 shows the ground truth material properties and the reconstructed TEE material properties. **Figure 1** shows the line profile across different materials. From Table 1 and Figure 1, we observe the following: (1) At 100 keV, the Rayleigh cross-section is significantly smaller than the Compton cross-section. (2) The percentage error in the Rayleigh cross-section is higher than that of the Compton cross-section, due to the relatively low number of Rayleigh events resulting from its smaller cross-section. (3) The ratio σ_r / σ_c preserves the relative ranking of different materials. (4) The estimated $Z_{eff,\ R/C}$ by TEE is close to the ground truth value calculated using equation (11).

Head phantom

In the second experiment, a head phantom is placed at (0, 0, 310 mm)**.** The X-source is mono-energetic at 100 keV. The cone beam originating from the source has a half-angle of 12 degrees. The image pixel size is 1 mm × 1 mm × 1 mm.

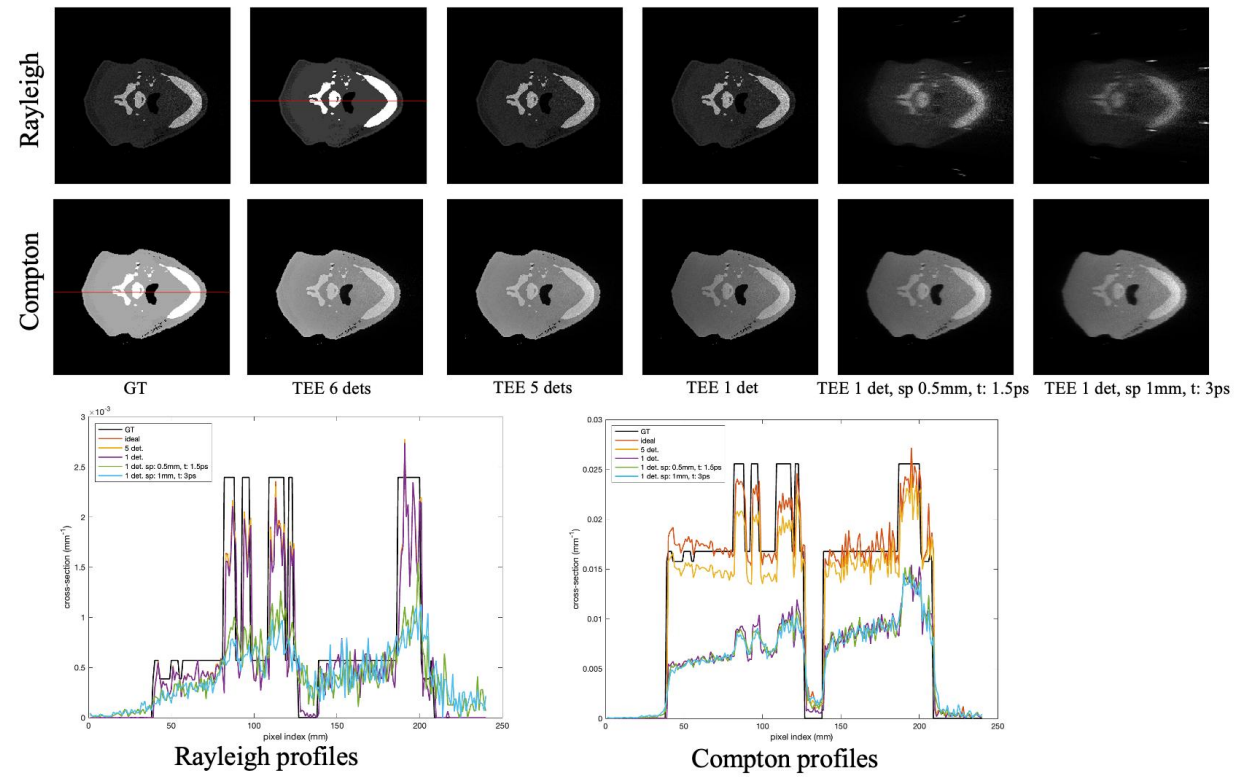


Figure 2. TEE reconstructed Rayleigh and Compton images of the head phantom with varying detector, spatial, and temporal resolution. (Bottom) Profile comparison. The top and bottom rows show the images and profiles, respectively.

In this experiment, the LAC map is treated as a known prior for attenuation correction. In practical applications, the LAC map can be estimated from a prior CT scan. **Figure 2** presents the TEE-reconstructed Compton and Rayleigh images. From these results, we observe: (1) Reconstruction using five detectors is comparable to that using six detectors, as scatter photons traveling opposite the beam direction have very low counts and contribute minimally to image formation. Specifically, the detectors in the experiments accounts for 77.5%(front), 4.1%(back), 4.5%(side), 4.1%(side), 4.7%(side), 5.1%(side) of the arriving photons. (2) When only one detector is used, a substantial number of scatter photons are lost, causing more noticeable image degradation. In addition, the posterior side of the phantom appears darker than in the six-detector case due to lost backward-scatter photon counts. (3) Reduced spatial-temporal resolution leads to additional blurring, since inaccurate photon arrival time and position result in less precise estimation of scatter origin. Other than that, the results are consistent with the slab phantom experiment, that the Raleigh scatter and Compton scatter cross-sections can be separately reconstructed. Moreover, Raleigh scatter cross-section has a higher soft tissue contrast that reflects the material Z_{eff}.

The bottom row of Figure 2 shows the line profile of TEE reconstruction. When it has 5 or 6 detectors, the estimated Rayleigh and Compton cross sections closely align with the ground truth. However, when it has only 1 detector, it dramatically underestimates the cross sections.

Micro phantom

In the third experiment, a tissue slice phantom of size 4mm × 4mm × 4mm was placed at (0, 0, 310 mm). The X-source is poly-energetic with 120 kVp. The cone-beam starting from the source has a half-angle of 1 degree. The image pixel is of size 0.1 mm × 0.1 mm × 0.1 mm. For this experiment, we did not apply path attenuation correction during the imaging due to negligible attenuation from the small phantom size. It reconstructs a high-resolution scatter image with combined Rayleigh and Compton scatters.

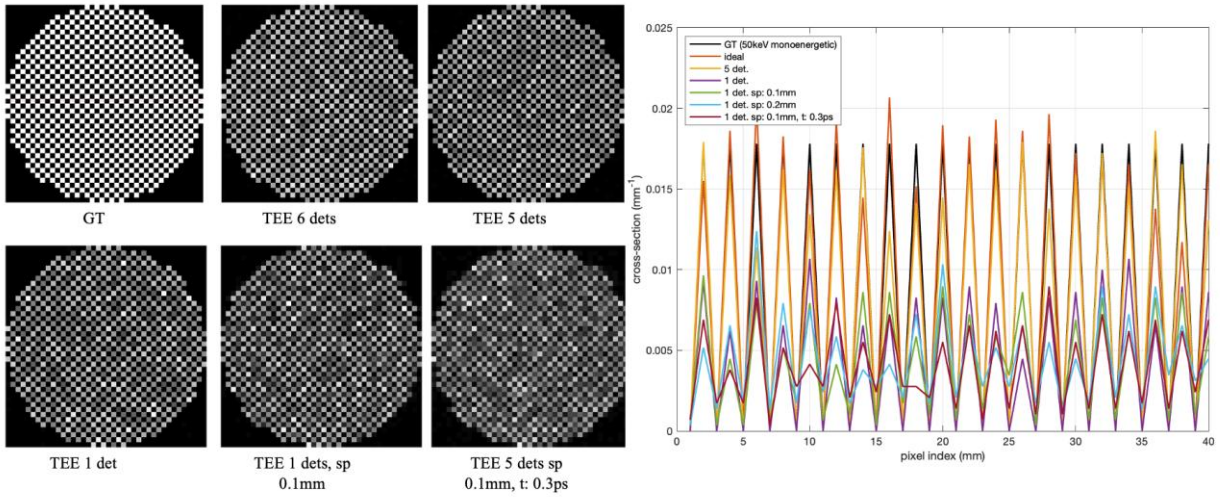


Figure 3 TEE reconstructed scatter images of the checkerboard phantom.

Figure 3 shows the reconstructed scatter images of the checkerboard phantom. Like the observations in the previous experiments, more detectors and higher resolution lead to superior quantification of the imaging intensity. However, even with a single detector (0.1 mm spatial resolution, 0.3 ps time resolution), the system is able to accurately recover the high-resolution patterns.

Figure 3 shows the line profile of the TEE reconstructed scatter images of the checkerboard phantom. From this figure, we can see that the reconstruction with 6 and 5 detectors matches the ground truth value. With only one detector, many scatter photons are not recorded, thus underestimating the photons. Furthermore, when the resolution is lower, the scatter cross section at the dark space is overestimated, resulting from inaccurate scatter location calculation.

Discussion

This paper presents a theoretical study on utilizing the ToF and energy information of individual scattered photons to reconstruct the scattering cross-section of objects. In contrast to conventional CT, which relies solely on primary photons to reconstruct the linear attenuation coefficient (LAC), the proposed approach leverages the rich information embedded in scattered photons. With a theoretical monoenergetic and ps-pulsed X-ray source, and a high-speed single-photon detector with energy and time resolution, we distinguished between Rayleigh and Compton scattering based on the measured energy of the scattered photons. This enabled the generation of separate Rayleigh and Compton scatter images, offering enhanced material characterization and effective atomic number quantification, which can be used for soft tissue differentiation [20]. In addition, the proposed TEE CT eliminates the need for rotating the X-ray source and detector, which could allow 3D image acquisition where X-ray projections from multiple angles are impossible. Moreover, eliminating mechanical components can be beneficial for high-resolution image acquisition, where resolution is limited by rotating components [21]. Another notable advantage of TEE CT is its exceedingly low imaging dose, which is ~1/100 of conventional CT for 3D imaging. Unlike conventional Compton scatter imaging without Time-of-Flight (ToF) data—which is typically restricted to resolving coarse object outlines [14–16]—TEE possesses the theoretical potential to produce detailed, high-resolution 3D images. Also, due to the extremely efficient utilization of photons, TEE can reconstruct images with extremely low doses, e.g., 50μGy as shown in our simulation. Furthermore, this approach differs from the previous work[22] which utilizes ToF data primarily to reject, rather than analyze, scattered photons.

The analysis is performed under the following idealized assumptions: (1) a fully enclosed detector capable of capturing all scattered photons, (2) sufficiently high spatial resolution, (3) sufficiently high temporal (ToF) resolution, and (4) sufficiently high energy resolution, (5) LAC of the objects for the slab phantom and head phantom and (6) perfectly pulsed and/or monochromatic X-ray source (monochromatic X-ray is only needed

for the separation of Compton and Rayleigh). In practice, the requirement of a fully enclosed detector box can be approximated by using a limited number of detectors positioned to cover the majority of scattering angles, with the results scaled accordingly based on the observed scatter events. As shown by the results, the detector in the opposite direction of the beam direction can be omitted in most cases without noticeable effects. To achieve a target spatial resolution of approximately 1 mm, the detector's spatial resolution should be of the same order. Correspondingly, the ToF resolution should be around 3 ps, which translates to a path length uncertainty also on the order of 1 mm. Our complementary experimental results suggest that using detectors with 1 mm spatial resolution and 3 ps ToF resolution does not significantly degrade image quality compared with the ideal scenario. The LAC images for attenuation correction of the TEE images can be obtained either from previous images of the subject or jointly as part of the TEE reconstruction process. If the LAC images are acquired using poly-energetic X-rays, dual-energy CT methods can be employed to estimate mono-energetic LAC images[23]. Similar to PET/CT systems, the LAC image in this context does not need to be highly accurate for the purpose of path attenuation correction.

For the results of the head phantom, we additionally scaled the output from the proposed algorithm, since Geant4 handles particle interactions internally with certain approximations [24,25]. Specifically, we multiply the reconstructed image by a constant to minimize the square error between the ground truth and the scaled reconstruction. When many dense objects, such as bones, are present, the results are underestimated. The underestimation is particularly evident in the Rayleigh-scatter images.

It is worth noting that knowledge of the Rayleigh and Compton scattering cross-sections, along with the LAC, enables material and elemental decomposition through solving systems of linear equations. However, the sensitivity of such decomposition is often a concern. For instance, elements such as carbon (C), nitrogen (N), and oxygen (O) exhibit very similar scattering profiles due to their proximity in the periodic table, leading to ill-conditioned and highly sensitive linear systems.

TEE CT provides enhanced contrast for soft tissues that exhibit similar linear attenuation coefficients (LACs) but differ in their effective atomic numbers (Z_{eff}). Recall that TEE reconstructs the Rayleigh and Compton scattering cross-sections once a preliminary LAC image is available. Previous studies [26] have shown that the ratio between Rayleigh and Compton cross-sections is approximately proportional to the material's Z_{eff}. Consequently, TEE can generate a scaled representation of the Z_{eff} distribution.

Moreover, TEE introduces an additional *dimension of interaction* to the measurement space. Conventional dual- or multi-energy CT enhances imaging quality or material decomposition by varying photon energies. In contrast, TEE differentiates photon–matter interactions—namely, Rayleigh, Compton, and photoelectric effects (the latter estimated by subtracting Rayleigh and Compton contributions from the total LAC). By combining multiple energies, it can further boost the material decomposition and image quality.

Time-of-flight (ToF) information has been leveraged for image reconstruction. In PET-CT, for example, the difference in the arrival times of the two coincident 511 keV annihilation photons has been used to estimate the location of the annihilation event along the line of response to improve resolution [27,28] or for reconstruction free PET[29]. Currently, temporal resolution ~100 ps has been achieved in practical PET systems [30]. A significant push for 10 ps resolution is underway [31,32]. Compared with PET, which focuses on 511 keV photons, TEE detects photons of much lower energy that alleviate some of the technical challenges in achieving both temporal and energy resolution. The other challenge is the X-ray source. Commonly available hot cathode X-ray sources have pulse width ~ ms [33], which is too long for TEE. Photocathode X-rays using pulse light and a photocathode to produce pulsed electrons for high-speed imaging. Photocathode X-ray sources with sub 100 ps pulse widths are commercially available. Sub ps pulses have been demonstrated in experimental conditions [34]. Alternatively, inverse Compton scattering X-ray sources, which transfer the energy from electrons to visible light via head-on collision, not only can achieve sub-ps pulse width, but also near monochromatic energies that are ideal for TEE imaging [35–37]. Therefore, although significant challenges still remain, TEE as a novel imaging modality is worth further research and development.

In conclusion, the paper demonstrates a theoretical framework for a novel Time and Energy encoded-CT (TEE-CT) interrogating the full time and energy information of scatter photons. The feasibility of TEE-CT is validated on a tissue slab phantom, a head and neck phantom, and a micro phantom with high resolution patterns. The results show the reconstruction of Rayleigh and Compton scatter images from a single projection without moving components. At the same time, the resultant images preserve geometrical accuracy and resolution.

Methods

General setup and Monte Carlo simulation

The general Monte Carlo simulation setups are illustrated in **Figure 4**. In a 3D coordinate system, the X-ray source is located at $\mathbf{x_s = (0, 0, -290\ mm)}$, which emits cone-beams to the phantom. There are, by default, six (**1 m × 1 m**) detectors **500 mm** to the origin enclosing the whole volume. We assume ideal detectors, which absorb and record position, energy, and time-of-flight of all arriving photons. At each time, one or a few photons are emitted at the same time along the same direction. The photon transportation and interaction with the phantom were then simulated using Geant4 with the following configuration.

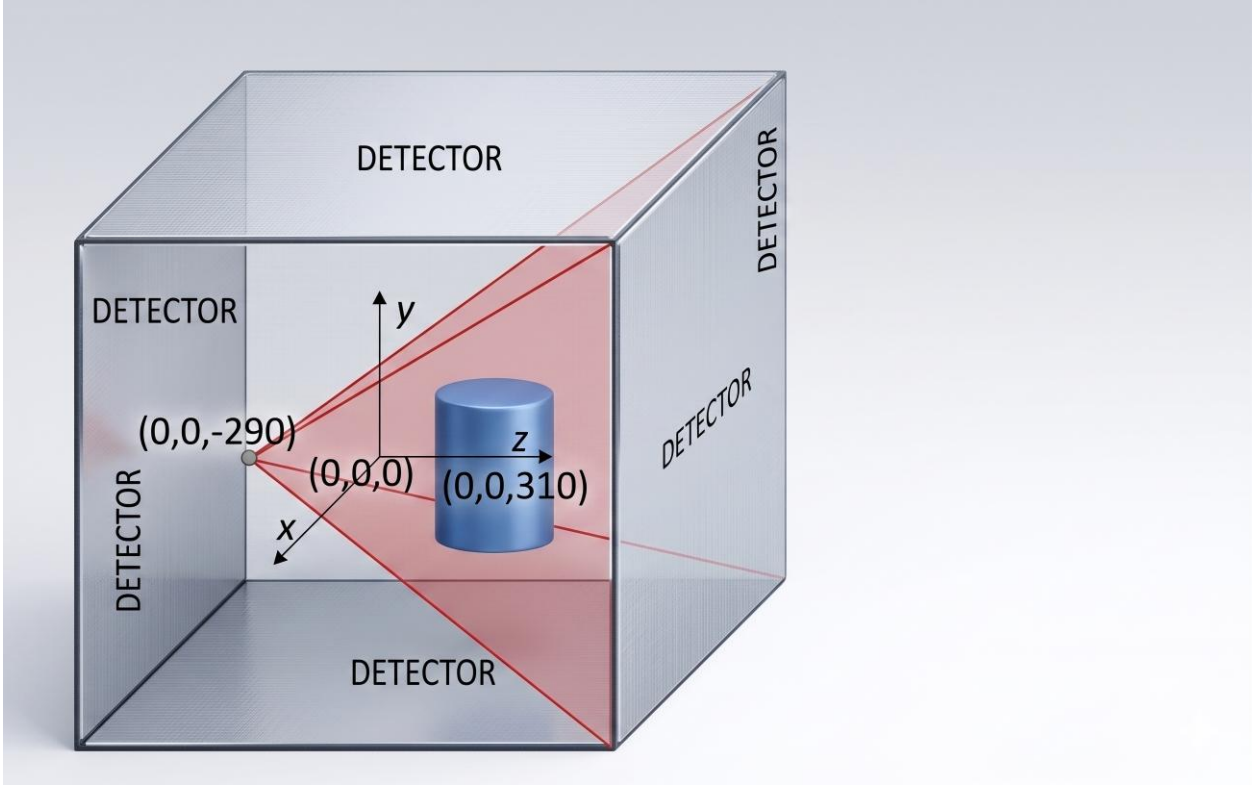


Figure 4. Experimental setup. The scanning object and X-ray source are enclosed in a cube, whose six sides are X-ray detectors. The 3D image is acquired via a single exposure without rotating the X-ray source or the detectors.

The initial position and direction of each photon emitted from the X-ray source were input into Monte Carlo for transportation calculation. The arrival position and the ToF were then determined at the detector. Using this information and assuming that each detected scattered photon results from a single-scatter event, we estimate the scatter location within the volume. By counting the number of scattering events occurring in each voxel, a 3D scatter distribution map was reconstructed. We first review the theoretical framework of conventional CT reconstruction, which serves as a basis for the subsequent description of TEE reconstruction.

Other information about photon energy, phantom, resolution, and beam is detailed separately for each different experiment.

A Review of Conventional CT Reconstruction

Conventional CTs, including fan-beam and code-beam CT, aim to reconstruct the linear attenuation coefficient (LAC) μ: $\mathbb{R}^3 \to \mathbb{R}$ of an object. In a typical setup, an X-ray source and a detector rotate around the object to record the intensity of beams along varies of paths through the volume. For each path $\ell \in \boldsymbol{\mathcal{L}}$, the associated beam intensity $N(\ell)$ follows a Poisson distribution

$$N(\ell) \sim Poisson(N_0(\ell)e^{-y(\ell)}) \quad (1)$$

where $N_0(\ell)$ is the initial intensity of the beam along the path ℓ, and $y(\ell)$ denotes the path integral of μ

$$y(\ell) \triangleq \int_\ell \mu(s)ds \quad (2)$$

In conventional reconstruction, an estimated path integral $\tilde{y}(\ell)$, is computed as

$$\tilde{y}(\ell) = -\log\frac{N(\ell)}{N_0(\ell)} \quad (3)$$

The reconstruction process is typically formulated as a linear inverse problem, where the goal is to find μ that minimizes the discrepancy between $A(\ell)$ and $\tilde{y}(\ell)$, with A representing the Radon transform, a linear operator that maps LAC μ to the estimated path integral $\{\tilde{y}(\ell)\}_{\ell \in \mathcal{L}}$.

In practice, the X-ray source is often polyenergetic, emitting photons over a range of energies. The above formulation assumes a constant energy spectrum throughout the beam's propagation. As a result, the model effectively captures the average attenuation behavior, enabling accurate reconstruction under the monoenergetic assumption. When large attenuation or dense objects present, the condition can be violated, resulting in beam hardening artifacts [38] if the spectral shift is not compensated.

Time-energy-encoded (TEE) CT Reconstruction

Reconstruction Process

In TEE CT, we collect the following information of each individual arriving. 1) Starting position $x_s \in \mathbb{R}^3$: This is the same as the position of the X-ray source. 2) End position $x_e \in \mathbb{R}^3$: The end position can be acquired when

a photon hits the detector. The accuracy of this value depends on the detector resolution. 3) Initial direction z $\in \mathbb{R}^3$: The initial direction of the photon can be controlled by adopting beams toward different directions sequentially. 4) Time of flight t $\in \mathbb{R}$: It is the time from the photon emission to the detection. 5). Initial energy $E_{ini} \in \mathbb{R}$: The initial energy of photons, which we assume monogenetic in this study. 6) Energy E $\in \mathbb{R}$: The arriving photon's energy recorded by the detector. The accuracy of this value depends on the detector's energy resolution.

In the following, we propose a method to leverage the information from individual photons for reconstruction. We assume that all scattered photons result from single-scatter events and estimate the scatter cross-section for each voxel. Specifically, we parameterize the scatter location as $\boldsymbol{x}_{sca} = \boldsymbol{x}_s + a\boldsymbol{z}$, with $a \in \mathbb{R}_+$. Given ToF t and the speed of light c, we have the equation related to the photon path length $a + \|\boldsymbol{x}_e - \boldsymbol{x}_s - a\boldsymbol{z}\| = ct$. The solution of the equation is

$$a = \frac{c^2t^2 - \|\boldsymbol{x}_e - \boldsymbol{x}_s\|^2}{2(ct - \langle \boldsymbol{x}_e - \boldsymbol{x}_s, \boldsymbol{z}\rangle)}, \tag{4}$$

and therefore

$$\boldsymbol{x}_{sca} = \boldsymbol{x}_s + \frac{c^2t^2 - \|\boldsymbol{x}_e - \boldsymbol{x}_s\|^2}{2(ct - \langle \boldsymbol{x}_e - \boldsymbol{x}_s, \boldsymbol{z}\rangle)}\boldsymbol{z} \tag{5}$$

The scatter cross-section can be estimated by counting the scatter events happening in each voxel. It is important to note that the frequency of detected scatter photons depends on the scatter cross-section of voxels, the fluence of voxels, and the path attenuation. Therefore, the following correction must be applied to the increment to account for the effect of path attenuation. Formally, let σ be the vector representing the scatter cross-section of the voxelized object and i be the index of the voxel containing $\boldsymbol{x}_{sca}$, then for all paths $\ell: \boldsymbol{x}_s \to \boldsymbol{x}_{sca} \to \boldsymbol{x}_e$, we have

$$\sigma[i] = \sum_{\ell: scatters\ at\ voxel\ i} \exp\left(\int_\ell \mu(s)ds\right) / \phi[i] \tag{6}$$

where ϕ[i] is the fluence of voxel i in the blank field. Suppose prior knowledge of LACs map is available, e.g., from CT, the path integral in the equation can be calculated with ray-tracing algorithms. The reconstruction process is summarized as the following algorithm

---

Algorithm 1 Reconstruction Process

1: **Inputs:** Collection of detected events $\{(\boldsymbol{x}_s, \boldsymbol{x}_e, \boldsymbol{z}, t)\}$, blank field fluence map ϕ, prior knowledge of LAC map $\boldsymbol{\mu}$

2: **Initialization:** Scatter image $\sigma[i] = 0$ for all i, where i indexes voxels.

3: **for** $(\boldsymbol{x}_s, \boldsymbol{x}_e, \boldsymbol{z}, t)$ from all recorded events **do**

4: $\quad \boldsymbol{x}_{sca} = \boldsymbol{x}_s + \frac{c^2t^2 - \|\boldsymbol{x}_e - \boldsymbol{x}_s\|^2}{2(ct - \langle \boldsymbol{x}_e - \boldsymbol{x}_s, \boldsymbol{z}\rangle)}\boldsymbol{z}$

5: **if** $\boldsymbol{x}_{sca}$ is outside the volume or $\frac{\boldsymbol{x}_e-\boldsymbol{x}_s}{\|\boldsymbol{x}_e-\boldsymbol{x}_s\|} = \boldsymbol{z}$ **then**
6: **continue**
7: **end if**
8: Compute path integral $I = \int_{\ell:\boldsymbol{x}_s\to\boldsymbol{x}_{sca}\to\boldsymbol{x}_e} \mu(s)ds$
9: i = FindVoxel($\boldsymbol{x}_{sca}$)
10: $\boldsymbol{\sigma}[i] \leftarrow \boldsymbol{\sigma}[i] + \exp(I)/\boldsymbol{\phi}[i]$
11: **end for**
12 **return** $\boldsymbol{\sigma}$

If a mono-energetic X-ray source is used, Rayleigh and Compton scatter photons can be further distinguished by examining whether the energy of the scattered photon changes. This allows for the separate reconstruction of Rayleigh and Compton scatter images, enhancing tissue contrast. Specifically, if $(\boldsymbol{z}, \boldsymbol{x}_s, \boldsymbol{x}_e, E_{ini}, E)$ corresponds to a Rayleigh event, then

$$\sigma_{Rayleigh}[i] \leftarrow \sigma_{Rayleigh}[i] + \exp(I)/\boldsymbol{\phi}[i]. \quad (7)$$

If $(\boldsymbol{z}, \boldsymbol{x}_s, \boldsymbol{x}_e, E_{ini}, E)$ corresponds to a Compton event, then

$$\sigma_{Compton}[i] \leftarrow \sigma_{Compton}[i] + \exp(I)/\boldsymbol{\phi}[i]. \quad (8)$$

In the next section, we elaborate on how to decide the interaction types.

Rayleigh and Compton Images

The Rayleigh and Compton scatter cross-sections can be reconstructed separately if mono-energetic X-ray source applied. Specifically, for a scatter photon, if the arriving photon energy E equals to the initial energy E_{ini} then it is considered a Rayleigh scatter; otherwise, it is considered Compton scatter. We provide the following pseudocode to differentiate primary, Rayleigh scatter and Compton scatter photons.

Algorithm 2 Interaction Type

1: **Inputs:** $\boldsymbol{z}, \boldsymbol{x}_s, \boldsymbol{x}_e, E_{ini}, E$
2: **if** $\frac{\boldsymbol{x}_e-\boldsymbol{x}_s}{\|\boldsymbol{x}_e-\boldsymbol{x}_s\|} = \boldsymbol{z}$ **then**
3: **return**: "primary"
4: **end if**

5: Calculate $\boldsymbol{x}_{sca} = \boldsymbol{x}_s + \frac{c^2t^2 - \|\boldsymbol{x}_e - \boldsymbol{x}_s\|^2}{2(ct - \langle \boldsymbol{x}_e - \boldsymbol{x}_s, \boldsymbol{z} \rangle)} \boldsymbol{z}$

6: **if** $\boldsymbol{x}_{sca}$ is outside the volume **then**
7: **return:** None
8: **end if**
9: **if** $E = E_{ini}$ then
10: **return** "Rayleigh"
11: **end if**
12 **if** E aligns with the result of Klein-Nishina formula then
13: **return** "Compton"
14: **else**
15: **return**: None
16: **end if**

It should be noted that the estimated Rayleigh image is subject to bias, as multiple-scatter events can be erroneously misinterpreted as single-scatter events, leading to an overestimation of the Rayleigh scattering cross-section. This occurs when the scattering location inferred from the detected energy and time-of-flight (ToF) lies within the phantom, even though the detected photon has undergone multiple scattering. Nevertheless, the simulation results indicate that the effect is negligible, as Rayleigh scattering events are relatively rare within the imaging energy range, and multiple-scattering events occur much less frequently than single-scattering events (approximately scaling with higher powers of the Rayleigh scattering probability). For example, in our head-phantom experiment, the single, double, and triple Rayleigh-scatter photons account for 95.58%, 4.26%, and 0.16%, respectively, of the total Rayleigh-scatter photons arriving at the head. In contrast, the estimate for the Compton image is unbiased, as the selection criterion requires the detected energy to match the theoretical prediction from the Klein–Nishina formula. This effectively excludes multi-scatter and photoelectric events.

Compton scattering is closely related to electron (and thus mass) density, while Rayleigh scattering has a more complex relationship with the material's atomic number. However, the ratio of Rayleigh scattering to Compton scattering can be used to determine the effective atomic number Z_{eff} [39]. The separate reconstruction of two images thus leads to significantly improved material differentiation, especially for soft tissues with similar LAC but different Zeff.

Z_{eff} serves as a representative value that characterizes how a compound or mixture interacts with photons as if it were a single-element material. The definition of Z_{eff} depends on the interaction we are interested in. Given that the cross sections of Rayleigh and Compton are approximately proportional to Z^2, Z, their Z_{eff} can be defined as

$$Z_{eff,Rayleigh} = \sqrt{\frac{\sum_i w_i/A_i \times Z_i^2}{\sum_i w_i/A_i}} \quad (9)$$

$$Z_{eff,Compton} = \frac{\sum_i w_i/A_i \times Z_i}{\sum_i w_i/A_i} \quad (10)$$

Where w_i is the mass fraction of the element. The Zeff of σ_r / σ_c can be defined as

$$Z_{eff,R/C} = \frac{\sum_i w_i/A_i \times Z_i^2}{\sum_i w_i/A_i \times Z_i} \quad (11)$$

The reconstruction pipeline was tested on three phantoms: a slab phantom consisting of heterogeneous materials, a head and neck phantom, and a micro phantom with high-resolution checkerboard patterns.

Funding

The work is supported in part by NIH R01EB031577 and R01CA255432.

Author contributions: [Authors to provide and verify individual contributions before submission.]
Competing interests: [Authors to confirm and complete before submission.]
Additional information

1. The study does not involve animal or human subjects. Clinical trial: NOT APPLICABLE.
2. Consent to Publish declaration: not applicable.
3. Ethics and Consent to Participate declarations: not applicable.

Data availability

The datasets used and/or analysed during the current study are available from the corresponding author on reasonable request.

References

1. Swinehart, D. F. The Beer-Lambert Law. *J. Chem. Educ.* **39**, 333 (1962).
2. Willemink, M. J. & Noël, P. B. The evolution of image reconstruction for CT—from filtered back projection to artificial intelligence. *Eur Radiol* **29**, 2185–2195 (2019).
3. Hsieh, J. *Computed Tomography: Principles, Design, Artifacts, and Recent Advances*. (SPIE Press, 2003).
4. Aichinger, H., Dierker, J., Joite-Barfuß, S. & Säbel, M. *Radiation Exposure and Image Quality in X-Ray Diagnostic Radiology: Physical Principles and Clinical Applications*. (Springer-Verlag, Berlin, Heidelberg, 2011). doi:10.1007/978-3-642-11241-6.
5. Patel, T., Peppard, H. & Williams, M. B. Effects on image quality of a 2D antiscatter grid in x-ray digital breast tomosynthesis: Initial experience using the dual modality (x-ray and molecular) breast tomosynthesis scanner. *Med Phys* **43**, 1720 (2016).

6. Hattori, H., Yatagawa, T., Ohtake, Y. & Suzuki, H. Learning Scatter Artifact Correction in Cone-Beam X-Ray CT Using Incomplete Projections with Beam Hole Array. *J Nondestruct Eval* **43**, 99 (2024).

7. Ritschl, L., Fahrig, R., Knaup, M., Maier, J. & Kachelrieß, M. Robust primary modulation-based scatter estimation for cone-beam CT. *Med Phys* **42**, 469–478 (2015).

8. Zhu, L., Bennett, N. R. & Fahrig, R. Scatter correction method for X-ray CT using primary modulation: theory and preliminary results. *IEEE Trans Med Imaging* **25**, 1573–1587 (2006).

9. Swindell, W. & Evans, P. M. Scattered radiation in portal images: a Monte Carlo simulation and a simple physical model. *Med Phys* **23**, 63–73 (1996).

10. Bootsma, G. J., Verhaegen, F. & Jaffray, D. A. Efficient scatter distribution estimation and correction in CBCT using concurrent Monte Carlo fitting. *Med Phys* **42**, 54–68 (2015).

11. Rossignol, J. *et al.* Time-of-flight computed tomography - proof of principle. *Phys. Med. Biol.* **65**, 085013 (2020).

12. Tashima, H. *et al.* 3D Compton image reconstruction method for whole gamma imaging. *Phys Med Biol* **65**, 225038 (2020).

13. Tashima, H. & Yamaya, T. Compton imaging for medical applications. *Radiol Phys Technol* **15**, 187–205 (2022).

14. Arendtsz, N. V. & Hussein, E. M. A. Energy-spectral Compton scatter imaging. I. Theory and mathematics. *IEEE Transactions on Nuclear Science* **42**, 2155–2165 (1995).

15. Arendtsz, N. V. & Hussein, E. M. A. Energy-spectral Compton scatter imaging. II. Experiments. *IEEE Transactions on Nuclear Science* **42**, 2166–2172 (1995).

16. Redler, G. *et al.* Compton scatter imaging: A promising modality for image guidance in lung stereotactic body radiation therapy. *Medical Physics* **45**, 1233–1240 (2018).

17. Kwon, S. I. *et al.* Ultrafast timing enables reconstruction-free positron emission imaging. *Nat. Photon.* **15**, 914–918 (2021).

18. Schwartz, F. R. *et al.* Photon-Counting CT: Technology, Current and Potential Future Clinical Applications, and Overview of Approved Systems and Those in Various Stages of Research and Development. *Radiology* **314**, e240662 (2025).

19. Kuroda, R. *et al.* Present Status of Photo-Cathode RF Gun System and its Applications. in *Proceedings of the 2005 Particle Accelerator Conference* 710–712 (2005). doi:10.1109/PAC.2005.1590536.

20. Lyu, Q., Neph, R. & Sheng, K. Tomographic detection of photon pairs produced from high-energy X-rays for the monitoring of radiotherapy dosing. *Nat Biomed Eng* **7**, 323–334 (2023).

21. Ruf, M., Lee, D. & Steeb, H. A multifunctional mechanical testing stage for micro x-ray computed tomography. *Rev. Sci. Instrum.* **94**, 085115 (2023).

22. Rossignol, J. *et al.* Time-of-flight computed tomography - proof of principle. *Phys Med Biol* **65**, 085013 (2020).

23. Yu, L., Leng, S. & McCollough, C. H. Dual-Energy CT–Based Monochromatic Imaging. *American Journal of Roentgenology* **199**, S9–S15 (2012).

24. Shirmardi Sp, M. M. Comparison of Geant 4, MCNP Simulation Codes of Studying Attenuation of Gamma rays through Biological Materials with XCOM and Experimental Data. *J Appl Computat Math* **03**, (2014).

25. Al Kanti, H., Arectout, A., El Hajjaji, O., El Bardouni, T. & Al Mugahed, M. Validation and investigation of mass attenuation Coeffcients calculations in different parts of adult human body organ using GAMOS code. *Radiation Physics and Chemistry* **239**, 113271 (2026).

26. Duvauchelle, P., Peix, G. & Babot, D. Effective atomic number in the Rayleigh to Compton scattering ratio. *Nuclear Instruments and Methods in Physics Research Section B: Beam Interactions with Materials and Atoms* **155**, 221–228 (1999).

27. Alessio, A. M., Kinahan, P. E., Cheng, P. M., Vesselle, H. & Karp, J. S. PET/CT scanner instrumentation, challenges, and solutions. *Radiol Clin North Am* **42**, 1017–1032, vii (2004).

28. Kapoor, V., McCook, B. M. & Torok, F. S. An introduction to PET-CT imaging. *Radiographics* **24**, 523–543 (2004).

29. Kwon, S. I. *et al.* Ultrafast timing enables reconstruction-free positron emission imaging. *Nat. Photon.* **15**, 914–918 (2021).

30. Pourashraf, S., Cates, J. W., Innes, D. & Levin, C. S. Front-End Electronics for a 100 ps Coincidence Time Resolution TOF-PET Detector With 24-Fold LVDS Timing Channel Multiplexing. *IEEE Transactions on Instrumentation and Measurement* **73**, 1–14 (2024).

31. Lecoq, P. On the way to the 10 ps time-of-flight PET challenge. *Eur. Phys. J. Plus* **137**, 964 (2022).

32. Lecoq, P. *et al.* Roadmap toward the 10 ps time-of-flight PET challenge. *Phys. Med. Biol.* **65**, 21RM01 (2020).

33. Sato, E. *et al.* 10 kHz microsecond pulsed X-ray generator utilising a hot-cathode triode with variable durations for biomedical radiography. *Med Biol Eng Comput* **32**, 295–301 (1994).

34. Guo, Z. Ultrashort electron bunches with subfemtosecond jitter from an <math xmlns="http://www.w3.org/1998/Math/MathML" display="inline"><mi>X</mi></math>-band photocathode rf gun. *Phys. Rev. Accel. Beams* **26**, (2023).

35. Seipt, D. Narrowband inverse Compton scattering x-ray sources at high laser intensities. *Phys. Rev. A* **91**, (2015).

36. Graves, W. S. Compact x-ray source based on burst-mode inverse Compton scattering at 100 kHz. *Phys. Rev. ST Accel. Beams* **17**, (2014).

37. Hornberger, B., Kasahara, J., Ruth, R., Loewen, R. & Khaydarov, J. Inverse Compton scattering X-ray source for research, industry and medical applications. in *International Conference on X-Ray Lasers 2020* vol. 11886 51–60 (SPIE, 2021).

38. Hsieh, J., Molthen, R. C., Dawson, C. A. & Johnson, R. H. An iterative approach to the beam hardening correction in cone beam CT. *Med Phys* **27**, 23–29 (2000).

39. Duvauchelle, P., Peix, G. & Babot, D. Effective atomic number in the Rayleigh to Compton scattering ratio. *Nuclear Instruments and Methods in Physics Research Section B: Beam Interactions with Materials and Atoms* **155**, 221–228 (1999).